Full Length Article

Fuel-specific devolatilization parameters for detailed comparison of pulverized biomass fuels

Niko P. Niemelä [a],[*], Richard Nowak Delgado [c], Thorben de Riese [c], Henrik Tolvanen [a],
Sebastian Fendt [c], Hartmut Spliethoff [c], Tero Joronen [a],[b]

[a] *Materials Science and Environmental Engineering, Tampere University, Finland*
[b] *Valmet Technologies Oy, Lentokentänkatu 11, 33900 Tampere, Finland*
[c] *Chair of Energy Systems, Technical University of Munich, Germany*

ARTICLE INFO

ABSTRACT

Low-grade biomass feedstocks are sustainable alternatives for pulverized fuel applications in the energy industry. Adverse fuel properties can make their adoption challenging due to operational issues such as flame ignition problems and high emissions. These issues can be potentially resolved by Computational Fluid Dynamics (CFD) simulations, where a submodel is needed to describe the fuel devolatilization behavior. In this work, the devolatilization parameters are reported for three pulverized biomass fuels: high-quality industrial wood pellet, lower-grade spruce bark, and steam-explosion pretreated spruce bark. The parameters are determined with a combination of high heating-rate drop-tube reactor experiments and CFD-coupled optimization algorithm. Comprehensive analysis is conducted to examine how the devolatilization reactivity and steam-explosion pretreatment affect the industrially relevant fuel properties. The functionality of the drop-tube devolatilization parameters is further demonstrated in larger-scale combustion simulations of a 120 kW pulverized fuel test rig. The simulations are able to capture the more challenging ignition behavior of the lower-grade bark fuels, and give detailed insight on the phenomenological side of solid fuel ignition. The fuel devolatilization reactivity is shown to have a strong impact on highly nonlinear flame characteristics, such as NO formation. Most importantly, the presented characterization, simulation and analysis methods can be applied to other biomass feedstocks to better understand how reactivity is altered by feedstock pretreatment, and how the process characteristics are influenced by fuel devolatilization reactivity.

1. Introduction

Thermochemical conversion processes, such as pyrolysis, gasification and combustion, are viable technologies to produce renewable energy and fuels from biomass. Comprehensive review papers regarding the chemical, physical and modeling aspects of these processes can be found in [1–8]. A basic conversion step, devolatilization, is an integral part of all these technologies. The biomass decomposes chemically into gases, tars, and residual char mainly at temperatures above 250 °C [9]. In case of pyrolysis, the process itself coincides with devolatilization. To design efficient conversion technologies and to minimize emissions, it is important to characterize the devolatilization reactivity of different feedstocks. Ideally, the experimentally derived reactivity parameters can be used in the energy industry to examine how the biomass-specific properties affect the process performance, and finally, enable the

adoption of more challenging low-grade feedstocks as fuels. This might become more and more important in the future, as only the low-grade materials may be available to energy use. The high-quality biomass, such as core wood, may be used for the production of higher value products.

One commonly acknowledged challenge in the devolatilization studies is the strong influence of operating conditions on the kinetic parameters. The kinetic parameters derived for a same fuel by different research groups have shown significant variability, which has led to the questioning of the significance of solid fuel reactivity studies [10]. Some explanations for the varying results have been proposed, such as the heat and mass transfer limitations in the measurement devices, influenced for example by the different particle sizes and heating rates. The most commonly applied experimental device, thermogravimetric analyzer (TGA), can only reach maximum heating rates of the order of 1 K/s, whereas over 1000 K/s is characteristic for the industrial applications.

Nomenclature

A	Pre-exponential factor, 1/s
Bi	Biot number, –
c_p	Specific heat capacity, J/kg-K
d_{90}	Particle diameter at 90% in the cumulative distribution, m
E	Apparent activation energy, J/mol
$f_{ash,0}$	Mass fraction of ash in dry fuel particle, –
$f_{char,0}$	Mass fraction of char in dry fuel particle, –
$f_{vol,0}$	Mass fraction of volatiles in dry fuel particle, –
k	Reaction rate constant, 1/s
m_p	Particle mass, kg
$m_{s,in}$	Fuel sample mass fed into DTR, kg
$m_{s,out}$	Fuel sample mass collected at DTR outlet, kg
R_u	Universal gas constant (8.3145), J/mol-K
r	Radial distance from combustion chamber centerline, m
T_p	Particle temperature, K
t	Time, s
X	Mass loss of particle sample in DTR experiments, –
x	Axial distance, m

Greek symbols

ρ_p	Particle envelope density, kg/m^3

Abbreviations

CFD	Computational Fluid Dynamics
CPD	Chemical Percolation Devolatilization
DO	Discrete Ordinates radiation model
DTR	Drop-Tube Reactor
DPM	Discrete Phase Model
daf	Dry Ash-Free basis
db	Dry Basis
EDM	Eddy Dissipation Model
LES	Large Eddy Simulation
LF	Large fraction of fuel particles (300–355 μm)
LHV	Lower Heating Value
PSD	Particle Size Distribution
RANS	Reynolds-Averaged Navier–Stokes
SF	Small fraction of fuel particles (112–125 μm)
SFOR	Single First Order Reaction
TGA	Thermogravimetric Analyzer
UBC	Unburned carbon content in fly-ash
WSGGM	Weighted Sum of Gray Gases

For this reason, the reactivity parameters from TGA conditions may not apply in industrial applications [11,12]. Various high heating rate devices have been developed to overcome the issue, including wire mesh [13] and Drop-Tube Reactors (DTR) [14,15].

Computational Fluid Dynamics (CFD) modeling is rapidly gaining popularity as a design tool for thermal conversion systems, and the reactivity parameters derived from devolatilization experiments are extensively used by the CFD engineers, some examples including [16–20]. The reactivity parameters are typically taken from the literature, and have not necessarily been determined in similar conditions, or even for the same fuel, that are being simulated. While more and more sophisticated devolatilization models are constantly developed and compared in laboratory conditions, only a few studies have analyzed the impact on practical combustion simulations. In [21], biomass-coal co-combustion in pulverized fuel burner is simulated with Large Eddy Simulation (LES) technique, and different pyrolysis and char oxidation models are compared. In [22], the effect of devolatilization model on the aerosol particle formation in lignite combustion is studied. Both studies conclude that the flame properties are affected by devolatilization, but it is still unclear how strongly the industrially relevant factors, such as flame ignition, NOx emissions or particle burnout are influenced. In particular, the modeling has not matured to the level where different biomass feedstocks, or the effect of pretreatment methods, could be reliably compared in industrial applications. Considering the mentioned issues, it is an open question how beneficial it is to spend significant resources for measuring the fuel-specific reactivity parameters. In the author's opinion, a significant issue in the field is the lack of demonstration how the laboratory derived parameters scale up towards real simulation applications. Ideally, the functioning of new models or parameters should always be illustrated also for an application other than the measurement apparatus where they were derived from.

In this work, the devolatilization reactivity of three pulverized biomass fuels is compared. The reactivity parameters are determined with a CFD-coupled optimization algorithm introduced in our previous work [23]. It is based on high heating rate DTR measurement data, which is used by an optimization algorithm that is directly coupled to CFD models of the DTR, which mimic the experimental conditions as accurately as possible. A high quality industrial wood pellet is compared to a lower quality spruce bark, and its steam-explosion pretreated version. The bark is a side-stream from the pulp and paper industry, and
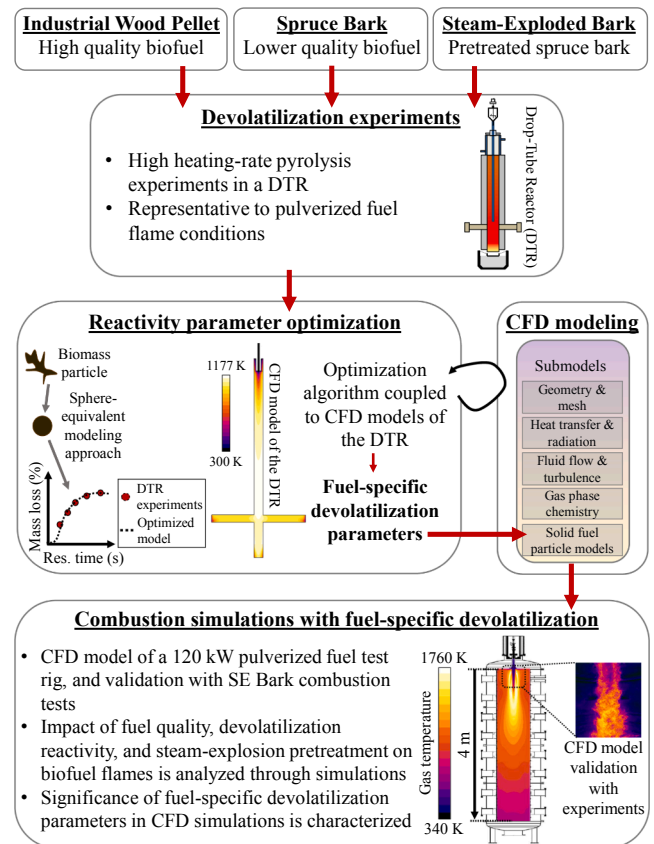

Fig. 1. Research methodology and main research topics.

is a good example of a sustainable lower grade biomass fuel. The three fuels are compared in combustion simulations of a 120 kW pulverized fuel test rig, where the bark and SE bark have also been combusted during the EU-funded Biofficiency research project. As such, the scalability of the devolatilization parameters from laboratory scale DTR towards the real combustion application is demonstrated. Furthermore,

Table 1
Ultimate and proximate analysis for the three fuels.

	Wood [23]	Bark [29]	SE Bark
	Ultimate Analysis, m-% dry basis		
C	49.4	49.4	53.7
O (by diff.)	43.1	40.2	35.4
H	6.2	5.8	5.7
N	<0.10	0.40	0.39
S	0.013	0.033	0.06
	Proximate Analysis, m-% dry basis		
Volatile matter	84.1	74.5	71.5
Char (by diff.)	15.1	22.3	23.8
Ash (815 °C)	0.8	3.2	4.7
LHV (MJ/kg)	18.36	18.52	19.95
Density (kg/m^3)	700	360	420

Fig. 2. Discrete and cumulative size distributions for the bark and SE bark as used in the DTR experiments and reactivity parameter optimization.

a comprehensive simulation study is conducted, where detailed analysis on the impact and significance of the devolatilization parameters is examined. At the same time, it is examined how the fuel quality, devolatilization reactivity and steam-explosion pretreatment affect the industrially relevant flame properties, such as NO emissions formation, and flame ignition.

2. Methodology

The methodology and research topics of this work are presented in Fig. 1. The basis of the study are the high heating-rate DTR test device and the CFD-coupled devolatilization model optimization procedure introduced in our previous work [23]. There, the devolatilization parameters were optimized for the industrial wood pellet which is used as a reference high quality biomass fuel in this work. Two additional fuels are characterized in this study. First one is the spruce bark which is a side-stream from the pulp and paper industry, and a good example of a sustainable lower grade biomass feedstock.

Second fuel is a pretreated version of the bark, which is produced through the steam-explosion process. It is a thermal pretreatment method comparable to torrefaction. However, in steam-explosion high-pressure steam reacts with the biomass. It increases the biomass energy density (MJ/kg) and improves the quality for transport and grinding. The product is a hard pellet, which is moisture resistant, and produces less dust in the handling processes [24]. Steam-explosion was originally patented for pulping in the 1926 [25], and the process equipment is similar that is applied in the Kraft Pulping [26]. It has been applied as a pretreatment for several biomasses, for instance, in the second generation bioethanol production [27]. Recently, the first commercial contract has been signed for providing a continuous process for steam-exploded black pellet production [28]. Thus, studying the combustion characteristics and enhancing the CFD modeling capabilities are of a high industrial interest.

The fuel-specific reactivity parameters are optimized for two particle size fractions of each fuel, to cover the behavior of the small and large fuel particles in industrial size distributions. The high heating-rate DTR device is used, because it can better represent the industrial flame conditions than TGA, and will presumably provide more realistic mass loss predictions for industrial CFD modeling applications.

A great number of reactivity parameters for different biomass fuels are reported in the scientific literature, but the functioning and scalability towards larger scale applications is rarely demonstrated. For this reason, the optimized reactivity parameters are further used in combustion simulations of a 120 kW pulverized fuel test rig. The CFD model is validated with comparison to test rig measurement data for the SE bark fuel. It is then used for a comprehensive simulation study, where detailed analysis on the impact and significance of the fuel-specific devolatilization parameters is conducted. The three fuels are compared and it is examined how the fuel quality, devolatilization reactivity, and steam-explosion pretreatment affect the industrially
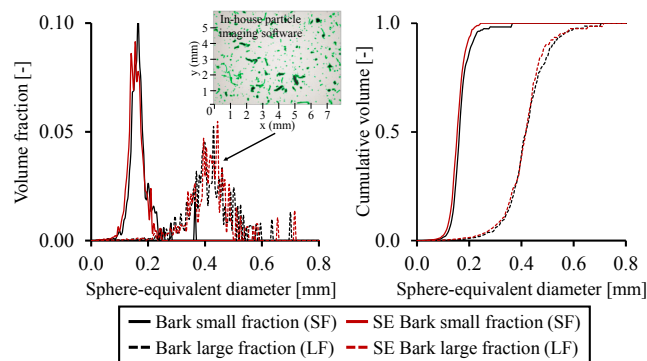
relevant flame properties, such as NO emissions formation and fuel ignition properties.

3. Experimental work

3.1. Fuel characterization

The ultimate and proximate analysis for the three fuels are presented in Table 1. All properties, except the densities, are measured with the laboratory methods that follow the EN, DIN, and ISO certified standards. The densities in Table 1 are not the standard bulk densities, as they are measured with a mercury porosimeter which provides the particle density as a function of pore size. It enables to determine the envelope density of individual fuel particles, which is used in the modeling applications. A cut-off pore size of 30 μm is used, which is considered as the resolution of an in-house particle imaging software, which is used for the particle size distribution measurements. As such, the bulk densities are lower and the intrinsic material densities are higher than the presented values.

Table 1 shows that the industrial wood pellet has the lowest ash content of the fuels, which indicates that it has the lowest slagging and fouling propensity. It also has the highest volatile matter and density, as well as the lowest nitrogen and sulphur contents. The lower quality bark has a similar heating value, but a considerably lower density than the wood. The steam-explosion pretreatment significantly reduces the bark's oxygen content, and increases the density and heating value, which are favorable effects considering the fuel quality. In grinding tests, it is observed that the SE bark pellets consume less energy than the fibrous wood, but the energy requirement is not much improved compared to the original bark.

As mentioned earlier, the DTR devolatilization experiments have been already conducted for the wood pellet in [23]. A similar experimental research chain is conducted here for the bark and SE bark. The fuels are ground into a fine powder like in pulverized fuel applications. The DTR devolatilization experiments are conducted for two particle size fractions in order to cover the behavior of different particle sizes in industrial size distributions:

1. Small size fraction (SF): particles collected between 112–125 μm sieves.
2. Large size fraction (LF): particles collected between 300–355 μm sieves.

The small fraction (SF) is chosen because it represents the smallest 10 m-% of the typical pulverized fuel size distributions in industrial applications. For the small particles, the internal heat transfer has minor effect on the devolatilization behavior (near thermally thin region, Bi < 100 in typical flame conditions). The large fraction (LF), on the other hand, is chosen because it represents the mass-average particle size in

industrial size distributions. These particles belong clearly in the thermally thick regime (Bi > 1000).

For the sieved size fractions, a sphere-equivalent particle size distribution is measured with an in–house particle imaging software. The software calculates the size distribution using 2D projections of a large number of particles in high resolution images. The size distributions for bark and SE bark are presented in Fig. 2, and are used later in the kinetic parameter optimization as discussed in Section 4.1.

3.2. Devolatilization measurements in drop-tube reactor

The electrically heated DTR can reach temperatures up to 1300 K. The maximum drop distance for the particles is 67.5 cm, which results in residence times between approximately 0.4 to 2.2 s for biomass particles between 1000 to 25 μm, respectively. The drop distance can be varied by adjusting the position of a water-cooled particle feeding probe inside the drop-tube. The particle heating rates can reach up to 10^4 K/s for small 100 μm range, and 10^3 K/s for large millimeter range. Different gas atmospheres can be fed through the reactor, and pure nitrogen is used in the pyrolysis tests of this study. Two nominal reactor temperatures, 973 K and 1173 K, are used for measuring the mass loss curves as a function of drop distance.

Before the experiments, the fuels are oven dried. A sample mass of 10–100 mg is weighted, dropped through the reactor, and collected into a liquid nitrogen -cooled collection vessel at the reactor outlet. The cold temperature of the vessel effectively stops the ongoing chemical reactions. The collected sample is weighted, and the sample mass loss X (–) for the particular drop distance is calculated as:

$$X = \frac{m_{s,in} - m_{s,out}}{m_{s,in}}, \tag{1}$$

where $m_{s,in}$ (kg) is the raw sample mass, and $m_{s,out}$ (kg) is the sample mass collected at the DTR outlet. A minimum of two samples is collected for each drop distance. In high enough drop distances, the mass loss remains constant and is defined as the high heating rate volatile content $f_{vol,0}$ (–) of the fuel. The residual char content $f_{char,0}$ (–) is calculated using the 815 °C ash content $f_{ash,0}$ (–) from the proximate analysis:

$$f_{char,0} = 1 - f_{vol,0} - f_{ash,0}, \tag{2}$$

The flow inside the reactor is kept laminar in order to avoid particle scattering to the reactor walls. Cold reactor tests have shown that the sample mass is well conserved after falling through the reactor. A camera based measurement device has been attached to the reactor in order to measure the particle falling velocities, and further to determine the particle residence times. Full details on the system can be found in references [30–32]. The experimental DTR data is used in the CFD-coupled optimization algorithm for determining the fuel-specific devolatilization parameters. The optimization procedure has been presented in details in our previous study [23], and is also further discussed in Section 4.1.

4. Numerical modeling

4.1. Optimization of fuel-specific devolatilization parameters

The fuel particles are modeled in the Lagrangian reference frame with the standardly used spherical modeling approach. In this section, only the devolatilization submodel is discussed, but a thorough description for all particle submodels and assumptions is given in Appendix A. Throughout this work, the simulations are conducted with the Ansys Fluent 2019 R3 CFD software. The particle mass loss in the devolatilization stage is calculated with the Single First Order Reaction (SFOR) model:

$$-\frac{dm_p(t)}{dt} = k[m_p(t) - (1 - f_{vol,0})m_{p,0}], \tag{3}$$

where k (s^{-1}) is the global rate constant, $f_{vol,0}$ (–) is the initial mass fraction of volatiles in the particle (obtained from the DTR experiments), and $m_{p,0}$ (kg) is the initial particle mass. The rate constant k is obtained from the Arrhenius equation:

$$k = Ae^{-(E/R_uT_p)}, \tag{4}$$

where A (s^{-1}) is the pre-exponential factor, E ($Jmol^{-1}$) is the apparent activation energy, and R_u ($Jmol^{-1}K^{-1}$) is the universal gas constant. It is an empirical model which describes the particle mass loss, and is not intended for detailed particle scale chemistry predictions. It has been used successfully in many combustion simulations, see e.g. [17–20], where the important contribution is to predict the release rate of volatiles in the correct location inside the flame/furnace. The motivation for using this models is its simplicity and fast calculation time, which makes it ideal for large scale industrial simulations and fast-pace R&D purposes. If the model is well fitted, it can predict comparable results with the more complicated models such as the Chemical Percolation Devolatilization model (CPD) [33]. Furthermore, the more complicated models are intentionally avoided in this work, because they usually require many detailed parameters that are difficult to measure, and become very cumbersome when many fuels are to be compared. In the end, there might be several unknown parameters that have to be inaccurately estimated for each fuel.

The devolatilization reactivity parameters, A and E in Eq. (4), are determined with the CFD-based optimization procedure [23]. The procedure is based on fuel particle mass loss calculations in 3D CFD models of the DTR test device. For each experimental drop distance, a corresponding CFD model is constructed which mimics the experimental conditions as accurately as possible. Each CFD model has boundary conditions, such as the wall temperature profile, based on measurements from the real reactor. The fuel particle trajectories through the reactor are simulated, and detailed temperature histories and mass loss profiles are obtained for the sample size distributions (see Fig. 2). The CFD modeled mass loss at the reactor outlet is compared to the experimental data, and a difference is calculated. The reactivity parameters are determined by minimizing this difference with a MATLAB optimization algorithm that is directly coupled to the CFD models of the DTR via Ansys as a server (AnsysAAS) coupling. The pre-exponential factor A and activation energy E are iterated as long as the best possible match between the modeled and measured mass loss is obtained.

The strength of the CFD-coupled procedure, as discussed in [14,23,34], is that the particle temperature histories and residence times can be accurately determined with the CFD models, including effects such as nonuniform reactor wall temperature, complicated radiative heat transfer to the particles, and different falling velocities and residence times for the different particle diameters. The reactivity parameters are optimized separately for the two size fractions (SF and LF) in order to account for the lower devolatilization rate of large particles due to internal heat transfer resistance. This approach is similar to the work presented in [35], where the apparent single-rate devolatilization kinetics are determined for different particle sizes using detailed mass transfer calculations and a multi-component devolatilization model. However, instead of fitting the parameters to another model, this work determines the apparent kinetics by a direct fit to the experimental DTR data.

4.2. CFD model of pulverized fuel test rig

The 120 kW pulverized fuel test rig is located at the Technical University of Munich, Germany. The test rig consists of a burner, and a combustion chamber with a diameter of 700 mm and a length of
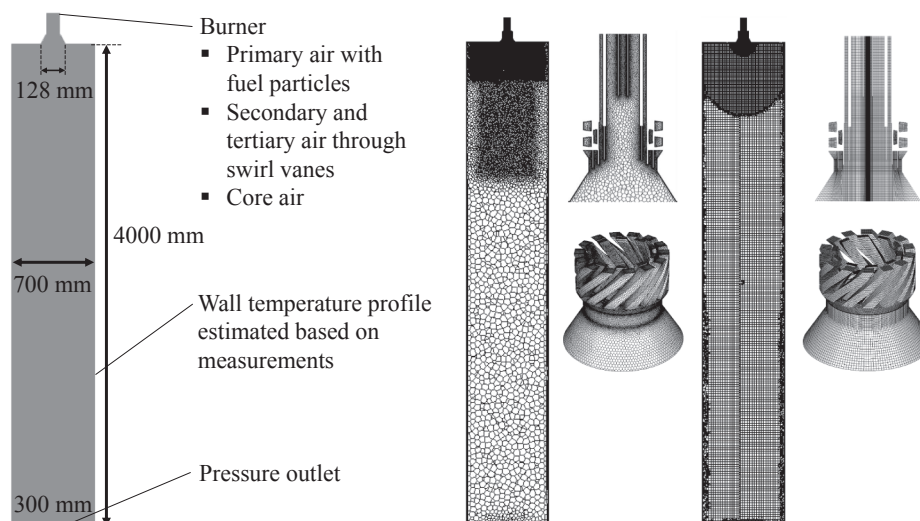
Fig. 3. 2D cutplanes showing the calculation domain and two example meshes. Swirl vanes shown in 3d view.

Table 2

Optimized devolatilization parameters for the two size fractions. Particle envelope density is determined with a mercury porosimeter. Volatile fraction, including sample standard deviation, is measured with DTR in 900 °C.

	Wood [23]		Bark		SE Bark	
	SF	LF	SF	LF	SF	LF
Single-Rate Devolatilization Parameters						
A (1/s)	5880	100	4350	1610	670	500
E (J/mol)	42 720	24 780	43 880	49 650	30 260	37 170
Particle properties for CFD, m-% dry basis						
Volatiles	94.2±1.4		89.4±3.0		80.7±2.5	
Char (by diff.)	5.0		7.4		14.6	
Ash (815 °C)	0.8		3.2		4.7	
ρ_p (kg/m³)	700		360		420	
c_p (J/kgK)	1500		1500		1500	

4000 mm. The fuel is fed into a top-down swirl burner by a gravimetric screw feeder system. A primary channel carries the biomass fuel via air stream, while additional preheated air is supplied into the core channel as well as into the swirled secondary and tertiary channels. The test rig is modeled as a 3D simulation domain including the swirl vanes and other important burner details. The domain and two computational meshes are illustrated in Fig. 3.

The simulations are conducted with a similar model set-up that is commonly used in the industrial scale simulations (see e.g. [17–20]). Because the large scale simulations are computationally expensive, the turbulence and combustion models have to be relatively simple to be suitable for fast-pace industrial design purposes. Therefore, the Reynolds-Averaged Navier–Stokes (RANS) approach is used. The fuel particles are modeled with the Lagrangian Discrete Phase Model (DPM) [36], using the optimized reactivity parameters in the devolatilization submodel. The gas-phase turbulence is modeled with the Realizable k-ε model, which is recommended for swirling flows [36]. The radiative heat transfer, including the scattering and absorption/emission of the particle phase, is modeled with the Discrete Ordinates (DO) model. The flue gas absorption coefficient is obtained from the Weighted Sum of Gray Gases (WSGGM) approximation. The Eddy-Dissipation Model (EDM) [37], combined with the Finite-Rate kinetics, is used for the calculation of gas-phase reaction rates. A two-step reaction mechanism, with CO intermediate, is used for the combustion of volatile gases that are released from the fuel particles. A thorough model description is given in Appendix A, where the submodels, equations, chemical reactions, kinetic parameters, model constants, and related assumptions

are presented in detail. It also includes a mesh independence study.

5. Results and discussion

5.1. Optimized devolatilization parameters

Table 2 presents the optimized reactivity parameters for the small and large size fractions (SF and LF) of each fuel. The parameters can be used in CFD modeling of high heating rate applications together with the other given particle properties. A specific heat capacity of $c_p = 1500$ J/kgK is recommended for all fuels, because the parameter optimization has been conducted with this value.

The SF parameters are recommended for small particles approximately in the range of $d_p \leqslant 200 \, \mu m$, whereas the LF parameters are recommended for larger than that. This diameter limit is based on the size distributions of DTR experiments (see Fig. 2). Both sets can be applied with the isothermal particle heat transfer equation that is the most common model in the CFD software. The LF parameters compensate for the nonisothermal effects and increase the particle devolatilization times as compared to the SF parameters. In our previous study [23], it was shown that a single LF parameter set was able to fit the experimental data of a large diameter range (from 500 up to 1000 μm for wood). Therefore, it is assumed that the single LF parameter set is suitable for all pulverized fuel particles larger than the small particle limit. The volatile contents in Table 2 are higher than the standard values presented in Table 1, because the high heating rate in DTR increases the devolatilized mass as compared to the standard low heating rate method. The steam-explosion pretreatment significantly reduces the high heating rate volatile content of bark (and increases the residual char content). The decrease in the volatile content is typical also for the torrefaction pretreatment [38].

The reactivity parameters in Table 2 are in agreement with the other high heating rate biomass devolatilization studies. Anastasakis et al. [13] have collected a wide range of reactivity parameters for various biomass fuels, including wood and lower grade feedstocks such as wheat straw and sunflower residues. The reported pre-exponential factors range typically from 8 to 40000 1/s, whereas the activation energies lie between 11 and 74 kJ/mol. As such, the values obtained in this study are well in line with the previous studies. Interestingly, the low heating rate studies (mostly with TGA) report much higher activation energies, typically from 100 to 200 kJ/mol [39]. The lower activation energies and pre-exponential factors, as also obtained in this study, seem to be a consistent result in high heating rate studies, but do not agree with the low heating rate methods.
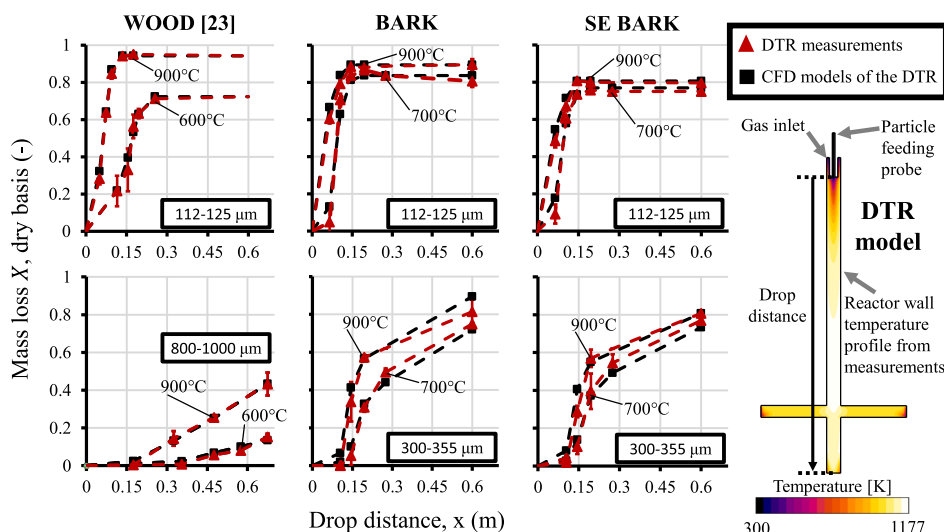
Fig. 4. DTR mass loss measurements compared to CFD simulations with optimized devolatilization parameters. Temperature contour of a DTR model shown on the right.
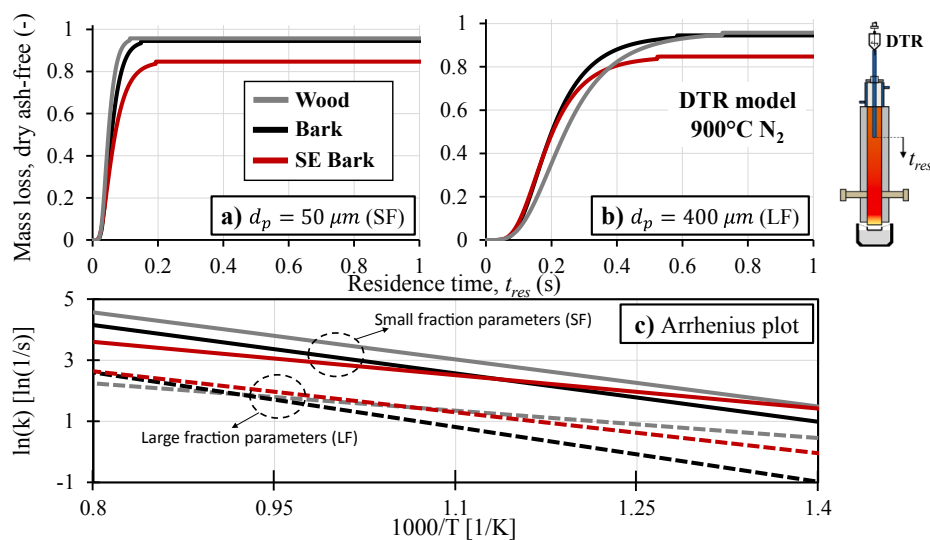

Fig. 5. a) and b): Wood, bark and SE bark mass loss profiles for two different particle sizes in the 900 °C nominal wall temperature in DTR CFD model. c): Arrhenius plot for the small (SF) and large fraction (LF) reactivity parameters of the fuels.

Fig. 4 shows the performance of the reactivity parameters against the experimental DTR data. The calculated mass loss values are obtained from DTR CFD models that mimic the experimental conditions as accurately as possible. Each experimental data point has its own corresponding CFD model, where the feeding probe is in the correct height and the wall temperature is set to the measured profile. Furthermore, the calculated values are averages over the simulated particle size distributions. Fig. 4 shows that despite using the relatively simple first order model, the optimized parameters are able to capture the experimental mass loss profiles very well for the different DTR setting temperatures and size fractions.

Fig. 5 presents the DTR mass loss profiles for two discrete diameters of 50 μm and 400 μm as a function of residence time. The residence time provides better comparability between the fuels than the drop distance used in Fig. 4, because the fuels have different falling velocities inside the reactor due to different densities. Graph a) shows that the 50 μm wood particle is the most reactive out of the three fuels. Despite having the highest density and volatile content, wood devolatilizes faster than the bark and SE bark. The SE bark is characterized by the significantly

slowest devolatilization, requiring 0.19 s compared to the 0.15 s of Bark and 0.11 s of wood. This can be a significant factor considering the fuel ignition behavior and flame stability, because the small particle volatiles are the primary ignition source in pulverized fuel flames. The results indicate that steam-explosion has a negative impact on the fuel reactivity. A similar trend has been shown to apply to torrefaction [38]. The significance of this reactivity decrease is analyzed in more details in Section 5.2, where the reactivity parameters are applied in the 120 kW pulverized fuel flame simulations.

Fig. 5 b) indicates that the relative differences between wood, bark and SE bark become less significant for the larger 400 μm particles. This may be related to the internal heat transfer limitations, which make the devolatilization process more heat transfer controlled than kinetically controlled. The wood particle devolatilization requires a slightly longer residence time, as it has the highest density and therefore the greatest particle mass to be heated and devolatilized.

The reactivity parameters of all fuels and size fractions are plotted in the Arrhenius plot in Fig. 5 c). It is important to note that the small particle rate curves are significantly above the large particle constituents
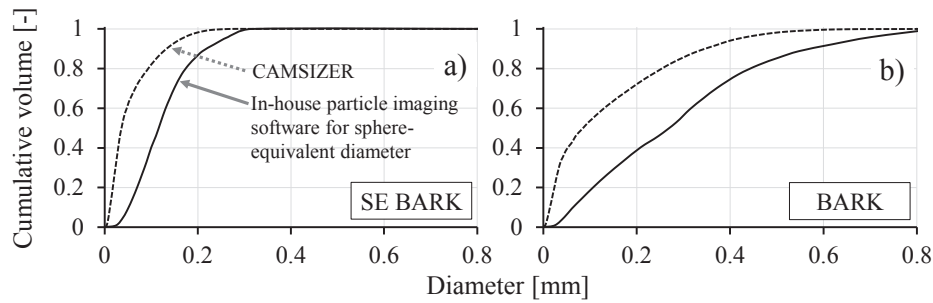
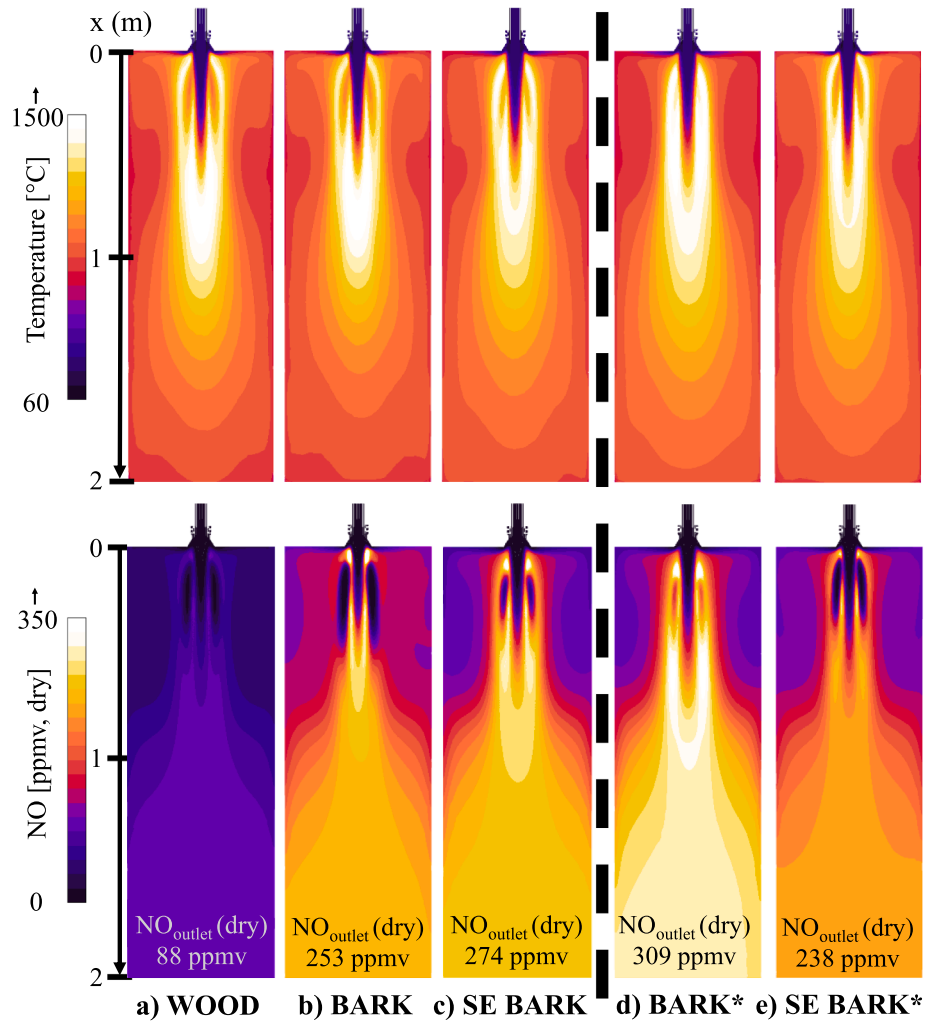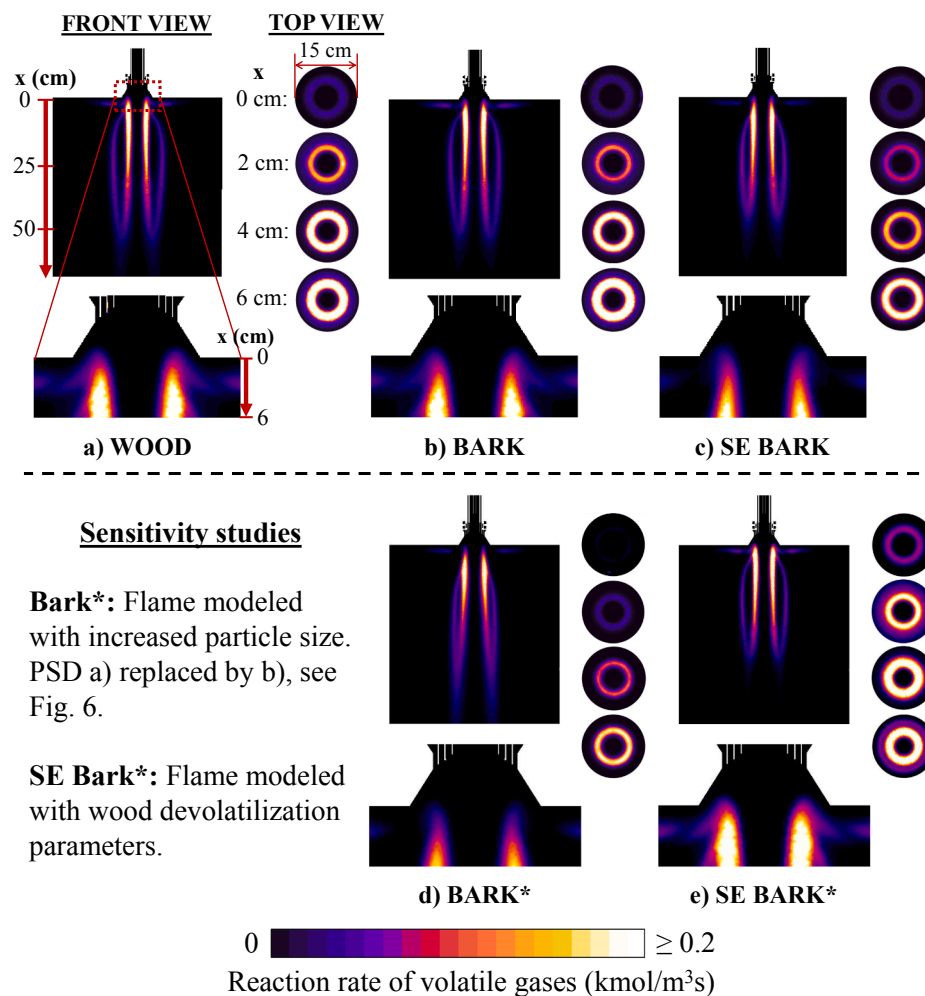Fig. 6. Bark and SE bark particle size distributions in experimental combustion tests and CFD simulations.

Fig. 7. a) to c): Comparison of temperature and NO fields in wood, bark and SE bark flames each having the same PSD. d): Increased particle size in bark simulation. e): Wood devolatilization parameters used for SE bark as a sensitivity study.

for all fuels. This means that the LF parameters predict much lower devolatilization rates and correctly capture the prolonged devolatilization times due to internal heat transfer resistance. The results strongly imply that the large biomass particles (approximately $d_p > 200\,\mu m$) cannot be modeled with the same reactivity parameters as the small nearly isothermal ones.

5.2. Devolatilization parameters in pulverized fuel flame simulations

In previous section, the devolatilization reactivities were compared in the laboratory scale DTR test device. This section examines how the optimized parameters scale up towards larger scale combustion simulation, and what kind of industrially relevant differences they can reveal between the analyzed fuels. Furthermore, the aim is to analyze how strongly the different flame properties, such as ignition and NOx formation, are influenced by the fuel quality and devolatilization reactivity. The 120 kW pulverized fuel test rig CFD model, described in detail in Appendix A, is used as a basis for this simulation study. The CFD model has been validated with an extensive measurement campaign for the SE bark fuel. The validation study is presented in Appendix B.

Fig. 8. a) to c): Combustion rate of volatile gases in wood, bark and SE bark flames, comparing the flame ignition characteristics for fuels with same PSD. d) and e): Sensitivity studies demonstrating how ignition is influenced by particle size distribution (Bark*) and devolatilization parameters (SE Bark*).

In the fuel comparison simulations, the fuel heat input, air–fuel ratio, particle size distribution (PSD), and air flow divisions between the different burner inlets are kept equal for all fuels. This way the influence of fuel devolatilization reactivity can be isolated from the other factors which affect the flame properties. Fig. 6 presents the PSDs that are used in the simulations, and have also been combusted in bark and SE bark combustion tests. The SE bark PSD in Fig. 6 a) is the main distribution used for the flame comparison purposes. The bark PSD in Fig. 6 b) is used for sensitivity studies as it includes significantly larger particle sizes. The PSDs have been obtained from two measurement devices: 1) the CAM-SIZER analyzer and 2) the in–house imaging software. The in–house tool measures larger diameters, because it determines the sphere-equivalent size which accounts for the high aspect ratio of biomass particles. It is used in the simulations, as the same tool has been applied in the devolatilization parameter optimization procedure. The sphere-equivalent PSD of Bark has not been measured by the in–house tool, but is estimated by assuming the same relative behavior between the CAMSIZER and in–house tool as measured for the SE bark.

The flame temperature and NO concentration fields for the three fuels are compared in Fig. 7 a) to c). Despite keeping most of the flame parameters constant, some local differences can be observed. The wood flame has the highest peak temperature, being approximately 60 degrees hotter than the bark and SE bark flames. Similar minor differences can be observed in the major gas concentration fields (CO_2, O_2, H_2O), which are not included in Fig. 7. The bark flame is very similar to the wood flame, whereas the SE bark flame is slightly longer and more detached

from the burner. The SE bark flame does not ignite as efficiently as the other two, because the high flame temperature is reached slightly further away from the burner.

The NO concentrations in Fig. 7 indicate larger variations between the fuels, but this can be mostly explained by the different fuel nitrogen contents, see Table 1. Many of the variations between the flames can be related to the different heating values, volatile contents, and C, H, O and N elemental compositions of the fuels. For example, the wood and bark have similar dry ash-free volatile contents and heating values, which explains the similarity of the flame temperature fields in graphs a) and b).

In order to explicitly isolate how the fuel devolatilization reactivity affects the biomass flame and simulation results, a sensitivity study is conducted by re-simulating the SE bark combustion with the wood reactivity parameters. The results are presented in Fig. 7 e), labeled as SE bark*. The SE bark* flame ignites closer to the burner and resembles more of the wood flame. The volatile release location has a large influence on the formed NO emissions, as it determines the local reaction conditions for the NO forming precursors (HCN, NH_3). The SE bark* simulation predicts as much as 13% lower NO emissions (238 ppmv dry) than the original SE bark simulation (274 ppmv dry), the original being closer to the measured value (278 ppmv dry). This indicates that the highly nonlinear flame properties, which are sensitive to local reaction conditions, require that the volatiles are released in the correct location inside the flame. In addition to NO emissions, this most probably applies to the modeling of alkali aerosol (as indicated also in [22]) and soot
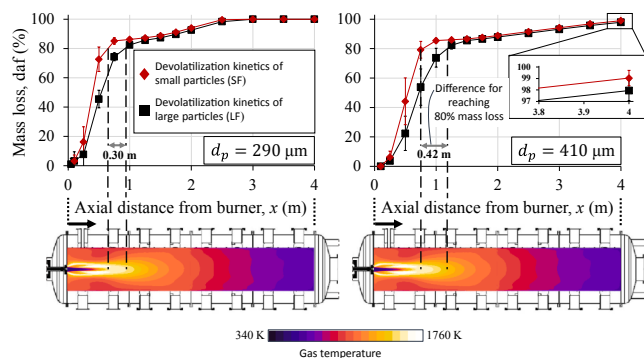
Fig. 9. Figure demonstrating how the small particle devolatilization parameters (SF, red curves) underestimate the pyrolysis distance as compared to the heat transfer compensated parameters (LF, black curves). Flame temperature contour shown below to illustrate the relative distances.

formation. Similar conclusions can be drawn from the sensitivity study for bark simulation, labeled as bark* (Fig. 7 d). In bark* simulation, the PSD has been increased from a) to b) of Fig. 6, which alters the volatile release location and results in higher NO emissions by 22% as compared to Fig. 7 b).

Flame ignition and stability issues are one of the most significant challenges in industrial pulverized fuel applications, when new feedstocks are considered for biomass heat/power plants or when coal plants are retrofitted to biomass. The previous sensitivity studies indicated that the fuel devolatilization reactivity has a large impact on the flame ignition position. Therefore, Fig. 8 presents a more detailed ignition comparison for the fuels. It shows the combustion rate of volatile gases from the front and top view angles of the flames. The contours for the first 6 cm after the burner outlet show that the wood flame a) ignites the most effectively and the bark flame b) is nearly as efficient. The SE bark flame c) needs at least 2 cm longer distance to reach similar combustion intensity as the wood and bark. This is a very significant lift-off distance if compared to the 12.8 cm burner mouth diameter.

The poor SE bark ignition is a direct effect of the low reactivity of small particles, as was hypothesized already in the discussion related to Fig. 5 a). The ignition issues are qualitatively supported by the SE bark combustion tests. Initially, the tests were attempted with larger particle sizes, but the flame was very unstable, easily detached from the burner, and had to be regularly re-ignited. The problem was solved only after the fuel was re-milled, resulting in the very fine powder shown in Fig. 6 a) ($d_{90} = 133\,\mu m$, CAMSIZER). The raw bark could be combusted with the much larger particle size of Fig. 6 b) ($d_{90} = 347\,\mu m$, CAMSIZER). Even though the RANS-type steady-state simulations cannot directly predict flame stability issues, the low reactivity of small SE bark particles, and the resulting ignition delay, can be interpreted as an explanation for the encountered problems. If the flame ignites far away from the burner, it can more easily escape downstream when a minor instability occurs (such as fluctuation in the fuel feeding rate into the burner). The bark* sensitivity simulation in Fig. 8 d) demonstrates that also the PSD has a significant effect on the ignition behavior. As such, the solid fuel ignition can be viewed as a combination of fuel devolatilization reactivity and the available PSD. The presented methods provide a predictive tool for analyzing the combined effect of these two factors.

The SE bark* sensitivity simulation in Fig. 8 e) shows that if wood devolatilization parameters are used for the SE bark, the simulation falsely predicts the most efficient ignition out of all fuels, which is merely a non-realistic result. This implies that the fuel-specific devolatilization parameters are needed for accurate ignition predictions. The results, overall, indicate that the optimization methodology attained in this work is able to provide fuel-specific information that can explain phenomenological and industrially relevant differences between biomass fuels. In many simulation studies, the fuel is modeled with

devolatilization parameters that are taken from the literature, and might have been determined for a different fuel or in different conditions (such as TGA) that prevail in the modeling application. Based on the results of this study, the main features such as major gas species and temperature field might be rather realistically predicted, but accurate ignition and NO (and presumably alkali aerosols and soot) require that the fuel-specific behavior is correctly captured.

As a final result, Fig. 9 illustrates the importance of using the internal heat transfer compensated LF parameters for the large fuel particles. The two parameter sets, SF and LF, are compared in the SE bark simulation by calculating the averaged axial mass loss profiles for two representative particle sizes, 290 μm and 410 μm, which belong in the LF size regime. With the SF parameters, approximately 30 cm ($d_p = 290\,\mu m$) and 42 cm ($d_p = 410\,\mu m$) shorter lengths are required to reach a 80 m-% (daf) mass loss as compared to the LF parameters. These are very large distances compared to the flame length that is shown in the temperature contours below. Too early volatile release can cause many errors in the CFD predictions, especially when the overall share of large particles is significant in the fuel size distribution (such as in full scale boiler simulations). Fig. 9 clearly implies that the large fuel particles cannot be modeled with reactivity parameters determined with small particle sizes.

Fig. 9 also indicates that the devolatilization parameters have a moderate impact on the final unburned fuel prediction. The 410 μm curves show that the predicted mass loss at the reactor outlet is 99.04 m-% (daf) with the SF parameters, and 97.95 m-% (daf) with the LF parameters. When translated to unburned carbon content (UBC) in the fly ash, the corresponding values are 16 m-% and 29 m-%, respectively. This implies that accurate devolatilization modeling is important if very precise UBC prediction is to be simulated. It is emphasized, however, that in general the char oxidation model is much more dominant for the final burnout prediction, because the oxidation is much slower compared to the devolatilization stage.

6. Conclusions and future work

This work determines and compares the fuel-specific devolatilization parameters of three pulverized biomass fuels. A high quality industrial wood pellet is compared to a lower quality spruce bark and its steam-explosion pretreated version. The presented methodology and the derived reactivity parameters can be used in the energy industry to examine how the biomass-specific properties affect the process performance, and finally, enable the adoption of more challenging low-grade feedstocks as fuels. The reactivity parameters are determined in a laboratory scale DTR test device and then used in combustion simulations of 120 kW pulverized fuel flames. The combustion simulations demonstrate the good scalability of DTR results towards the larger scale application. This is done because biomass devolatilization parameters are extensively published in the literature, but the added value for
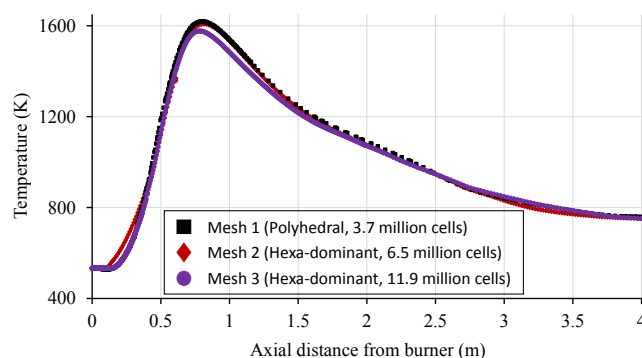
Fig. A.1. Combustion chamber centerline temperature profiles for three computational meshes.
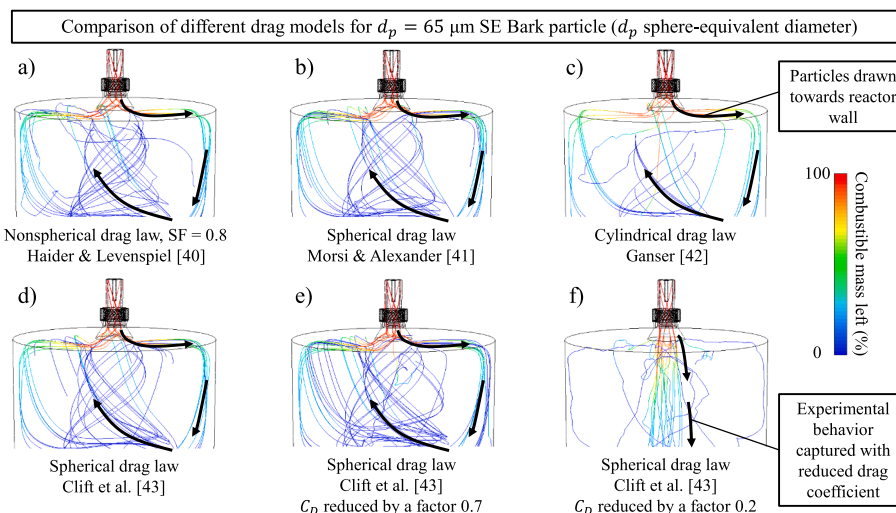
Comparison of different drag models for $d_p = 65\ \mu m$ SE Bark particle (d_p sphere-equivalent diameter)

a) Nonspherical drag law, SF = 0.8
Haider & Levenspiel [40]

b) Spherical drag law
Morsi & Alexander [41]

c) Cylindrical drag law
Ganser [42]

Particles drawn towards reactor wall

d) Spherical drag law
Clift et al. [43]

e) Spherical drag law
Clift et al. [43]
C_D reduced by a factor 0.7

f) Spherical drag law
Clift et al. [43]
C_D reduced by a factor 0.2

Combustible mass left (%)

Experimental behavior captured with reduced drag coefficient

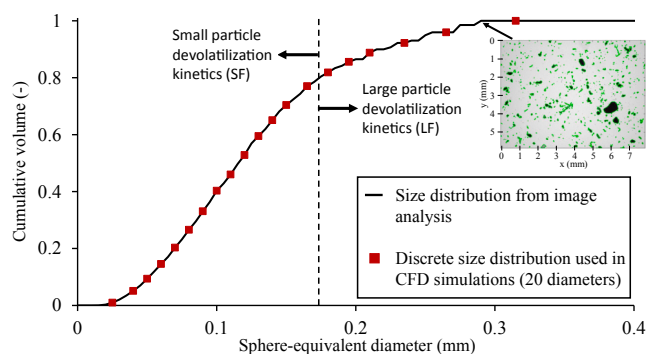**Fig. A.2.** Effect of drag law on the trajectories of 65 μm particles.

Fig. A.3. Sphere-equivalent size distribution for SE bark as burned in combustion tests and used in CFD simulations.

industrial applications has been unclear.

The steam-explosion pretreatment has many favorable effects on bark quality, such as increased density (+17%) and LHV (+8%). The produced pellet is more moisture resistant and produces less dust in the handling processes. On the other hand, the pretreatment has some

negative impacts on the fuel combustibility. The high heating rate volatile content is significantly reduced, and the devolatilization reactivity of small particles is decreased as compared to the raw bark. This is shown to have a negative impact on the flame ignition characteristics. As such, the SE bark needs to be ground into a finer dust for obtaining a stable flame. Most importantly, the presented characterization, simulation and analysis methods can be applied to other biomass fuels to better understand how the process characteristics are influenced by the fuel devolatilization reactivity, and also to quantify how the reactivity is altered by a feedstock pretreatment.

The fuel-specific devolatilization parameters can enable more detailed insight on biomass flame ignition. The ignition issues of SE bark combustion experiments were explained by the CFD simulation, which implied a more detached flame from the burner as compared to the wood and raw bark. The presented methods are shown to provide detailed information regarding the phenomenological side of solid fuel ignition, which is very difficult to study experimentally due to the very narrow localized nature. In addition to ignition, the fuel devolatilization behavior is shown to have a strong impact on the highly nonlinear flame properties, such as NO formation. This most probably applies also to alkali aerosol and soot formation, which are sensitive to the local reaction conditions where the volatiles are released. Finally, the

Instantaneous SE Bark flame
Image taken by infrared camera through glass window

Time-average SE Bark flame
Averaged from 200 instantaneous infrared images, temperature values only indicative

CFD simulation
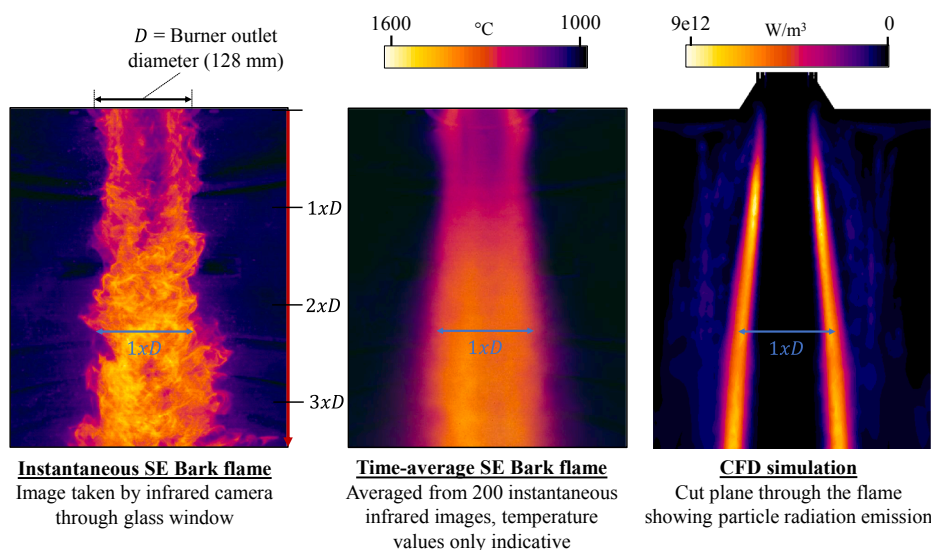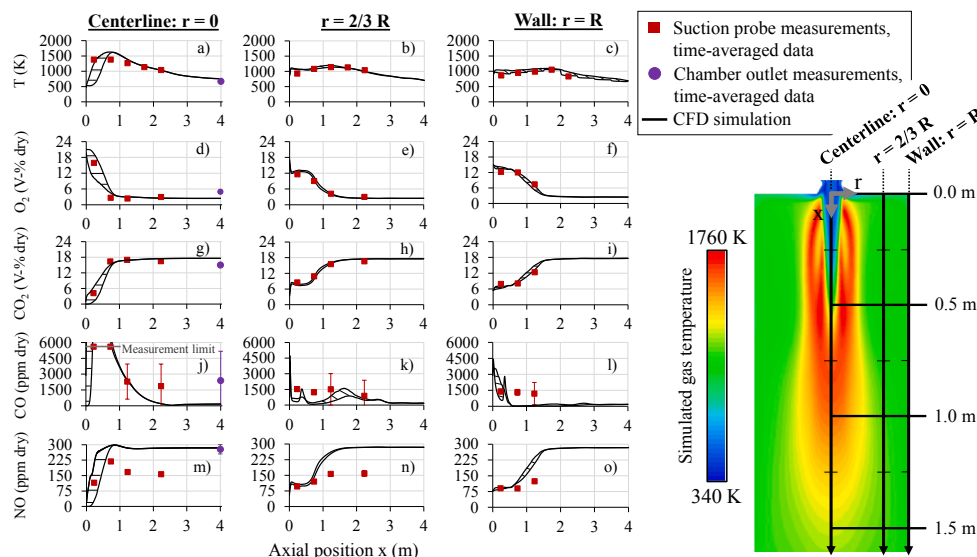Cut plane through the flame showing particle radiation emission

Fig. B.2. Thermal camera images compared to CFD modeling.

Fig. B.1. Measured axial temperature and gas profiles compared to CFD simulation results in three radial positions.

separately optimized large particle parameters, that compensate for the internal heat transfer resistance, are shown to be important for accurate prediction of unburned carbon in fly ash (UBC).

In future studies, a detailed ignition and flame stability analysis could be conducted using the fuel-specific reactivity parameters in transient Large-Eddy Simulations (LES). An important factor would be to model an industrial scale biomass boiler to illustrate how the conclusions scale up towards full-scale simulations. Finally, the determined parameters could be utilized in simulations of other high heating rate thermochemical conversion processes, such as the fast pyrolysis reactors and entrained flow gasifiers.

CRediT authorship contribution statement

Niko P. Niemelä: Conceptualization, Methodology, Software, Formal analysis, Investigation, Visualization, Writing - original draft. **Richard Nowak Delgado:** Conceptualization, Methodology, Formal analysis, Investigation, Writing - review & editing. **Thorben Riese:** Conceptualization, Methodology, Formal analysis, Investigation,

Writing - review & editing. **Henrik Tolvanen:** Conceptualization, Methodology, Writing - review & editing. **Sebastian Fendt:** Conceptualization, Methodology, Supervision, Funding acquisition, Writing - review & editing. **Hartmut Spliethoff:** Conceptualization, Methodology, Supervision, Funding acquisition. **Tero Joronen:** Conceptualization, Methodology, Supervision, Funding acquisition, Writing - review & editing.

Declaration of Competing Interest

The authors declare that they have no known competing financial interests or personal relationships that could have appeared to influence the work reported in this paper.

Acknowledgments

Appendix A. Detailed description of 120 kW test rig CFD model

This appendix presents a detailed description of the pulverized fuel test rig CFD model, including the mesh independence study, presentation of the fuel particle submodels, and finally a description of the gas-phase combustion modeling. The test rig is modeled with the ANSYS Fluent 2019 R3 CFD software [36] using a 3D simulation domain. The model includes the swirl vanes and other important burner details. The domain dimensions and two computational meshes are presented in the main article in Fig. 3. In total, three different meshes are tested in order to ensure mesh independent results. The largest mesh with 11.9 million cells is a hybrid tetrahedral/hexahedral mesh, in which the burner is a block-type structured hexahedral domain and the combustion chamber is an unstructured hexa-core domain. The second mesh is of a similar type with 6.5 million cells, and the third mesh is a fully unstuctured polyhedral mesh with 3.7 million cells. Fig. A.1 compares the reactor centerline gas temperature profiles for the three grids in SE bark simulation. All meshes predict similar profiles, the finest mesh producing a slightly lower maximum temperature. The polyhedral mesh is used in further calculations, as it is a good compromise between accuracy and relatively low total cell count. The convergence behavior is also very stable with the polyhedral mesh.

The fuel particles are modeled as spheres and their trajectories are calculated in the Lagrangian reference frame using the Discrete Phase Model (DPM) described in detail in [36]. The particle combustion process is modeled in three successive stages, where first the moisture evaporates, then the volatile gases are released, and finally the residual char (assumed as pure carbon) burns in surface reaction to CO, until the ash fraction remains. The particles are coupled to the Eulerian gas-phase equations through source terms, which are updated after 50 gas-phase iterations. Two-way coupling is assumed, meaning that the gas and particle phases can interact with each other (exchange momentum, heat and mass), but the particles cannot affect each other in any way (i.e. the particles cannot collide, or transfer heat or mass with each other). However, as the particles are coupled to the radiation model, they can indirectly transfer heat through radiation.

The trajectories are computed by integrating the force balance of Eq. (A.1):

$$\frac{d\vec{u_p}}{dt} = f_D(\vec{u} - \vec{u_p}) + \frac{\vec{g}(\rho_p - \rho)}{\rho_p},$$ (A.1)

where $\vec{u_p}$ (ms^{-1}) is the particle velocity vector, $\vec{u}$ (ms^{-1}) is the gas velocity vector, and ρ_p and ρ (kgm^{-3}) are the particle and gas densities, respectively. The second term on the right hand side is the force of gravity ($g = 9.81$ ms^{-2}), while the first term represents the drag force on the particle. Approximately 100 000 individual particle trajectories are calculated in order to obtain a representative sample of the fuel behavior and to evaluate the Eulerian source terms.

It is noticed that the simulation convergence is highly dependent on the trajectories of small fuel particles. Fig. A.2 presents the trajectories of twenty 65 μm particles calculated with various drag laws in Eq. (A.1). The nonspherical [40] and spherical drag law [41] are available in the Fluent 2019 R3 software, while the cylindrical [42] and spherical law [43] are implemented through user-defined functions. The general tendency with all models a) to d) in Fig. A.2, is that the particles are transported to the reactor wall after burner outlet (by the swirling secondary and tertiary flows). Because of this, a flame is not formed in the middle of the chamber and a converged solution is not obtained.

In the experiments, it is observed that the particles move axially downward after the burner outlet. Similar behavior is achieved in the simulation if the particle drag force is reduced as demonstrated in Fig. A.2 f). This reduced drag coefficient is used for the small fuel particles ($d_p < 170$ μm), while the larger ones are modeled with the nonspherical drag law [40] with a shape factor 0.8 (ratio between the surface areas of volume-equivalent sphere and actual particle). It is hard to find a reasoning for this behavior, but it is most probably related to phenomena that is not included in the modeling, such as particle collisions, clustering of small fuel particles, or a rocket force due to rapid volatile release. Some modeling inaccuracies can also be an explanation, such as erroneous particle-turbulence interaction modeling in the RANS simulation. In the author's experience, the drag reduction for small particles has also functioned well in pulverized biomass combustion simulations of other burners/boilers.

The particles heat up through radiation, and through convective heat transfer which is calculated from a Nusselt number correlation for sphere [44]. The particle energy equation is presented in Eq. (A.2):

$$m_p c_p \frac{dT_p}{dt} = hA_p(T_\infty - T_p) + \epsilon_p A_p \sigma(T_R^4 - T_p^4) - f_h \frac{dm_p}{dt} h_{char},$$ (A.2)

where m_p (kg) is the particle mass, $c_p = 1500$ (Jkg^{-1}K^{-1}) is the specific heat capacity, h (Wm^{-2}K^{-1}) is the convective heat transfer coefficient, A_p (m^2) is the spherical surface area, T_∞ (K) is the surrounding gas temperature, T_p (K) is the particle temperature, $\epsilon_p = 0.9$ (–) is the particle surface emissivity, σ is the Stefan–Boltzmann constant, $T_R = (G/4\sigma)^{1/4}$ (K) is the radiation temperature, and G (Wm^{-2}) is the incident radiation from the surroundings to the particle surface (obtained from the numerical radiation solution). The last term in Eq. (A.2) is active only in the final char oxidation stage. The constant f_h (–) is set to one, as recommended in the Fluent theory guide [36], which means the particles absorb 100 percent of the reaction heat h_{char} (Jkg^{-1}) that is released in the heterogeneous char combustion. A similar term is active in the initial water evaporation stage, but the reaction heat is replaced by the latent heat of water.

All particle sizes are calculated with the isothermal heat transfer model of Eq. (A.2). The temperature of large particles varies inside their volume and the single temperature value T_p is not sufficient to describe the real heating behavior. However, as the devolatilization reactivity parameters are optimized together with this equation, they compensate for the isothermal simplification and result in the correct mass loss rate in accordance with the DTR measurement data (so-called heat transfer compensated reactivity parameters). This procedure is considered appropriate, because the highly variable shapes, varying material properties, and internal temperature profiles cannot be accounted by any practical model. With the current optimization approach, all complicated effects can be lumped into the reactivity parameters. This procedure, as also proposed in [35,45], minimizes the computational requirements of the CFD simulation.

The equations for the mass loss calculations in the devolatilization step, as well as the reactivity parameter optimization procedure, are discussed within the main article. After the volatile mass has been released, the residual char burns in surface reaction to produce carbon monoxide. The apparent char oxidation rate is calculated with the widely used kinetics and diffusion limited surface combustion model (see [36]):

$$-\frac{dm_p(t)}{dt} = A_p p_{O_2} \frac{D_0 R}{D_0 + R},$$ (A.3)

where p_{O_2} (Pa) is the oxygen partial pressure in the surrounding computational cell, D_0 (sm^{-1}) is the diffusion-rate for oxygen towards the particle surface, and R (sm^{-1}) is the kinetic rate of char oxidation. The pre-exponential factor and activation energy for the kinetic rate R are assumed 0.002 s/m and 70 kJ/mol, respectively. These are otherwise the default values for coal in Fluent, but the activation energy has been reduced from 79 to 70 kJ/mol to account for the faster oxidation rate commonly measured for biomass chars. The diffusion rate D_0 requires a user-defined model constant C_1 (sK$^{-0.75}$). A reduced value of 2e-12 is used as recommended in [46] (5e-12 is the default in Fluent). The lower value prevents the particle temperature rising too high, which could result in too efficient char oxidation rate when the char gasification reactions are not accounted. Because this work concentrates on the devolatilization process, the char oxidation model is of a secondary importance. If highly accurate burnout results are needed, the char oxidation kinetics should be measured for the char in question, and the char gasification reactions could be included.

Fig. A.3 shows the particle size distribution of SE bark used in the 120 kW combustion tests. This sphere-equivalent size distribution is measured with the in-house particle imaging software and used in all CFD simulations (also for wood and bark). It is divided into 20 discrete particle diameters, which are each injected separately into the simulation domain. This enables choosing different devolatilization parameters for the different particle sizes. As shown in Fig. A.3, the diameters smaller than 170 μm are modeled with the SF reactivity parameters, and the larger with LF parameters (see Table 2). The cutoff diameter where the devolatilization parameters are changed is chosen based on the LF size distribution of DTR experiments (see Fig. 2).

The gas-phase solution is obtained numerically with the finite volume method by solving the Eulerian partial differential equations describing mass, momentum, species and energy conservation. The steady state pressure-based coupled solver is used. The gradients are estimated with the least-squares cell based method, the pressure is discretized with the PRESTO!-scheme, and the other variables with the second order upwind scheme. The pseudo transient method is used for additional convergence stability. The aforementioned equations and numerical solution methods are described in detail in many fluid dynamics books and in the theory guide of the CFD code [36]. The convergence is monitored by examining the residual levels, as well as multiple solution variables such as the outlet emissions and the temperature in a single point inside the flame. The simulations are considered

converged when the monitored values and residuals have stabilized, and the imbalance in overall mass and energy conservation are less than 0.5%.

The submodels are chosen such that a similar simulation set-up would be feasible also in industrial scale simulations. Because the large scale simulations are computationally expensive, the turbulence and combustion models have to be relatively simple to be suitable for fast-pace industrial design purposes. Keeping this in mind, the Reynolds-Averaged Navier–Stokes (RANS) approach is chosen. Turbulence is modeled with the Realizable k-ϵ model, which is recommended for highly swirling flows [36]. The radiative heat transfer, including the scattering and absorption/emission of the particle phase, is modeled with the Discrete Ordinates (DO) model. The absorption coefficient for the flue gas is obtained from the Weighted Sum of Gray Gases (WSGGM) model.

The Eddy-Dissipation Model (EDM) [37] combined with Finite-Rate kinetics is used as the combustion model. It determines a mixing-limited reaction rate from the turbulence parameters (k and ϵ). The finite-rate part calculates the Arrhenius-rate by using the mean species concentrations and temperature in the computational cells (thus not taking into account the effect of turbulent fluctuations). Finally, the combined model chooses the smallest of these rates as a controlling reaction rate in a cell. The advantage of the model is its simplicity, but the negative side is the fact that it requires two non-universal model parameters, A and B, which can have a large effect on the solution.

The applied reaction mechanism is presented in Eqs. (A.4)–(A.7). Eqs. (A.4) and (A.5) represent the gas release from the fuel particles during devolatilization and char oxidation, respectively. The volatiles are modeled with a lumped species, which for the SE bark is $C_{0.292}H_{0.508}O_{0.198}$. Its chemical composition and heating value are calculated from the ultimate and proximate analysis of Table 1. Thus, the volatile gas properties change according to the simulated fuel. The volatiles react in the gas-phase according to Eq. (A.6). The final reaction in Eq. (A.7) describes the CO oxidation.

The reaction rate for the volatile combustion in Eq. (A.6) is calculated solely with the mixing-limited rate of EDM (by setting Arrhenius activation energy to a low value). This is done because of convergence issues encountered with the Fluent's default Arrhenius rate (possibly because it is aimed for coal volatiles). Another modification is that the EDM constants A and B for the CO oxidation reaction (Eq. (A.7)) are set to values 2 and 0.25 (default 4 and 0.5), respectively. This lowers down the CO combustion rate, as recommended in [47].

$$\text{SEBark(s)} \xrightarrow{k} f_{vol,0}\text{Volatiles(g)} + f_{char,0}\text{Char(s)} + f_{ash,0}\text{Ash(s)} \tag{A.4}$$

$$\text{Char(s)} + \frac{1}{2}O_2 \rightarrow CO \tag{A.5}$$

$$C_{0.292}H_{0.508}O_{0.198} + 0.174O_2 \rightarrow 0.292CO + 0.254H_2O \tag{A.6}$$

$$CO + \frac{1}{2}O_2 \rightarrow CO_2 \tag{A.7}$$

The NO emissions are modeled similarly with the large scale boiler CFD studies (see e.g. [48]), including the thermal and fuel NO formation paths. The thermal NO is calculated using the extended Zeldovich mechanism, where partial equilibrium is assumed for O and OH radicals. The fuel NO formation is calculated assuming that 90 m-% of the fuel N content is released in the devolatilization stage. The composition of the volatile N is set as 57 m-% of NH_3, 3 m-% of HCN and 40 m-% of N_2, a trend shown in the experiments conducted for wood bark in [49]. The fuel nitrogen release in the char oxidation stage accounts for 10 m-% of the total fuel N content, consisting of 60 m-% of directly formed NO and 40 m-% of N_2. Finally, the released species react in the gas phase according to the $HCN/NH_3/NO$ reaction mechanism described in [36]. The effect of turbulent fluctuations is modeled with the probability density function method using the beta distribution with 20 discrete points, and the global maximum flame temperature as the upper limit. In the temperature levels of the current simulation, the fuel pathway has a more dominant role on the overall NO emissions.

Appendix B. CFD model validation with experiments

This appendix presents a general validation study for the CFD model of the pulverized fuel test rig. The test rig is located at the Technical University of Munich, Germany, where the combustion tests have been conducted during EU-funded Biofficiency research project. The raw bark and steam-exploded bark were tested in order to compare their combustibility. The main difference between the fuels was the more challenging ignition behavior of SE bark. The flame was initially very unstable, easily detached from the burner, and had to be regularly re-ignited. The problem was solved only after the fuel was re-milled into a much finer dust ($d_{90} = 133\,\mu m$ according to size distribution measurement with CAMSIZER). The raw bark, however, could be combusted with a stable flame with much larger particle sizes ($d_{90} = 347\,\mu m$, CAMSIZER) without any significant operating issues.

The SE bark flame was further characterized by an extensive measurement campaign in order to obtain more detailed validation data for CFD modeling. The gas temperatures were measured with an IFRF type suction pyrometer for accurate and radiation-independent temperature measurements up to 1800 °C. The pyrometer was inserted in one of the eight ports located axially at different heights in the combustion chamber, and positioned at the correct radial measurement location until a steady temperature measurement ($\pm$ 5 °C) was observed. Additionally, the gas composition was measured in two ways - with a suction probe for localized measurements (Siemens ULTRAMAT), as well as with a gas analyzer at the end of the combustion chamber (ABB AO 2020). With these analyzers, O_2, CO, CO_2 and NO were measured continuously during the experiments. The turbulent gas measurement data from ULTRAMAT was then time-averaged from a time period of 10–25 min of steady operation for each measurement point. The outlet concentrations from ABB AO 2020 were time-averaged over a longer period accounting the whole measurement campaign duration. Furthermore, an infrared video was recorded below the burner in order to monitor the flame shape and stability.

Fig. B.1 compares the SE bark CFD simulation and measurements. Axial profiles from the burner outlet ($x = 0$ m) down to the reactor outlet ($x = 4$ m) are presented at three radial positions, which are visualized in the embedded temperature contour. The CFD profiles (continuous lines) present the simulation values distributed around a three centimeter radius surrounding the measurement location (see the thin vertical lines in the contour plot). This is done because the measurement probe cannot be exactly positioned at the desired location, and a better comparison can be made when the distribution of CFD data is also shown.

A very good general correspondence for the simulation and measurements is implied by Fig. B.1. The temperature, O_2, CO_2, CO and NO profiles in graphs a) to o) have all relatively good match with measurements. However, various deviations can also be identified. The most notable are in the centerline temperature profile a), and in the CO and NO profiles j) to o). The temperature deviation for the burner outlet region in graph a) ($x < 1$ m) can be explained by the very sensitive measurement location. The embedded temperature contour shows that the temperature gradients are very large at the vicinity of the reactor centerline, and the pyrometer with relatively large suction head causes gas mixing when inserted inside the flame.

The reason for the deviation in the CO profiles j) to l), on the other hand, is explained by the problems experienced with the fuel feeding system during the combustion tests. Occasional high CO peaks occurred due to fluctuation in the fuel feeding rate (as seen from the high standard deviations), which greatly increase the time-averaged measurement values. During stable fuel feeding, the outlet CO concentration stayed well below 1000 ppm level, which is close to the CFD prediction at the reactor outlet. This problem was later solved by installing a vibrator to the fuel feeding system. The suction probe gas measurements were not reproduced after this, because the improved feeding system presumably had a negligible impact on the other gas species in Fig. B.1.

For the NO profiles in graphs m) to o), it is notable that the localized suction probe (Siemens ULTRAMAT) and the chamber outlet measurement (ABB AO 2020) indicate different NO levels. The deviation is most probably caused by a calibration error in the suction probe measurements. The maximum amount of fuel NO that can be formed in the simulation (based on the fuel nitrogen content and fuel NOx model settings) is approximately 660 ppm (dry). In this context, the CFD prediction is well in the correct range, and in a very good agreement with the outlet concentration measured by ABB AO 2020.

Fig. B.2 shows a qualitative comparison for the CFD simulation and thermal camera imaging of the SE Bark flame. An instantaneous infrared image is shown on the left, indicating the visual flame ignites at the burner mouth and burns very narrowly close to the combustion chamber centerline. The flame diameter is of the same order as the burner outlet (128 mm). The middle figure shows a time-averaged infrared image, which is processed by averaging the temperature values of each pixel in 200 instantaneous IR images, covering a total averaging time of 8 s. It is notable how symmetrical the time-averaged flame image is, especially when compared to the chaotic instantaneous flame on the left. The averaged IR flame closely resembles the RANS-type CFD results, where a time-averaged flow field is solved.

The right side of Fig. B.2 represents the CFD model, displaying the radiative heat source from the fuel particles in a middle cut-section of the flame. It is a good variable to be compared with the thermal camera images, which mostly capture the particle black-body radiation. It is emphasized that the CFD contour is a cut-plane through the flame, while the IR images are taken from the front of the flame (representing thermal radiation emitted by the whole flame volume). The infrared camera uses a fish-eye lens, which also slightly distorts the image dimensions. Therefore, a direct comparison cannot be made but some important conclusions can be drawn. Firstly, the CFD simulation predicts a very similar shape and size for the flame, indicating it captures the fuel particle stream relatively well compared to reality. Secondly, the CFD model indicates a high particle temperature at the flame edge and a colder temperature at the flame core, which can be also seen in the time-averaged IR image if carefully observed.

Despite of the discussed issues, it can be concluded that the SE bark simulation is able to accurately predict the important flame properties, such as the temperature, O_2, and CO_2 profiles which are remarkably similar to the measurements. The simulation is able to reproduce the measured data throughout the reactor volume. In particular, the accurate prediction of oxygen levels in all measured positions indicates that the volatile gas reactions, flame length, and the general flow field are well captured by the CFD model. This provides experimental confidence towards the test rig CFD model, and provides a good basis for the more theoretical simulation study conducted in the main paper.

References

[1] Sharma A, Pareek V, Zhang D. Biomass pyrolysis – A review of modelling, process parameters and catalytic studies. Renew Sustain Energy Rev 2015;50:1081–96. https://doi.org/10.1016/j.rser.2015.04.193.

[2] Wang S, Dai G, Yang H, Luo Z. Lignocellulosic biomass pyrolysis mechanism: a state-of-the-art review. Prog Energy Combust Sci 2017;62:33–86. https://doi.org/10.1016/j.pecs.2017.05.004.

[3] Dhyani V, Bhaskar T. A comprehensive review on the pyrolysis of lignocellulosic biomass. Renewable Energy 2018;129:695–716. https://doi.org/10.1016/j.renene.2017.04.035.

[4] Sansaniwal SK, Rosen MA, Tyagi SK. Global challenges in the sustainable development of biomass gasification: An overview. Renew Sustain Energy Rev 2017;80:23–43. https://doi.org/10.1016/j.rser.2017.05.215.

[5] Motta IL, Miranda NT, Filho RM, Wolf Maciel MR. Biomass gasification in fluidized beds: a review of biomass moisture content and operating pressure effects. Renew Sustain Energy Rev 2018;94:998–1023. https://doi.org/10.1016/j.rser.2018.06.042.

[6] Sankar G, Santhosh Kumar D, Balasubramanian KR. Computational modeling of pulverized coal fired boilers - a review on the current position. Fuel 2019;236:643–65. https://doi.org/10.1016/j.fuel.2018.08.154.

[7] Williams A, Jones JM, Ma L, Pourkashanian M. Pollutants from the combustion of solid biomass fuels. Prog Energy Combust Sci 2012;38:113–37. https://doi.org/10.1016/j.pecs.2011.10.001.

[8] Sahu SG, Chakraborty N, Sarkar P. Coal-biomass co-combustion: an overview. Renew Sustain Energy Rev 2014;39:575–86. https://doi.org/10.1016/j.rser.2014.07.106.

[9] Biagini E, Barontini F, Tognotti L. Devolatilization of biomass fuels and biomass components studied by TG/FTIR technique. Ind Eng Chem Res 2016;45(13):4486–93. https://doi.org/10.1021/ie0514049.

[10] White JE, Catallo WJ, Legendre BL. Biomass pyrolysis kinetics: a comparative critical review with relevant agricultural residue case studies. J Anal Appl Pyrol 2011;91:1–33. https://doi.org/10.1016/j.jaap.2011.01.004.

[11] Yin C, Yan J. Oxy-fuel combustion of pulverized fuels: combustion fundamentals and modeling. Appl Energy 2016;162:742–62. https://doi.org/10.1016/j.apenergy.2015.10.149.

[12] Mehrabian R, Scharler R, Obernberger I. Effects of pyrolysis conditions on the heating rate in biomass particles and applicability of TGA kinetic parameters in particle thermal conversion modelling. Fuel 2012;93:567–75. https://doi.org/10.1016/j.fuel.2011.09.054.

[13] Anastasakis K, Kitsiou I, de Jong W. Fast devolatilization characteristics of low cost biomass fuels, wood and reed. Potential feedstock for gasification. Fuel Process. Technol. 2016;142:157–66. https://doi.org/10.1016/j.fuproc.2015.10.018.

[14] Simone M, Biagini E, Galletti C, Tognotti L. Evaluation of global biomass devolatilization kinetics in a drop tube reactor with CFD aided experiments. Fuel 2009;88(10):1818–27. https://doi.org/10.1016/j.fuel.2009.04.032.

[15] Panahi A, Tarakcioglu M, Schiemann M, Delichatsios M, Levendis YA. On the particle sizing of torrefied biomass for co-firing with pulverized coal. Combust Flame 2018;194:72–84. https://doi.org/10.1016/j.combustflame.2018.04.014.

[16] Guo N, Llamas ADG, Li T, Umeki K, Gebart R, Løvås T. Computational fluid dynamic simulations of thermochemical conversion of pulverized biomass in a dilute flow using spheroidal approximation. Fuel 2020;271. https://doi.org/10.1016/j.fuel.2020.117495. 117495.

[17] Milićević A, Belošević S, Crnomarković N, Tomanović I, Tucaković D. Mathematical modelling and optimisation of lignite and wheat straw co-combustion in 350 MWe boiler furnace. Appl Energy 2020;260. https://doi.org/10.1016/j.apenergy.2019.114206. 114206.

[18] Wang X, Zhang J, Xu X, Mikulčić H, Li Y, Zhou Y, Tan H. Numerical study of biomass co-firing under Oxy-MILD mode. Renewable Energy 2020;146:2566–76. https://doi.org/10.1016/j.renene.2019.08.108.

[19] Holtmeyer ML, Kumfer BM, Axelbaum RL. Effects of biomass particle size during cofiring under air-fired and oxyfuel conditions. Appl Energy 2012;93:606–13. https://doi.org/10.1016/j.apenergy.2011.11.042.

[20] Black S, Szuhànszki J, Pranzitelli A, Ma L, Stanger P, Ingham D, Pourkashanian M. Effects of firing coal and biomass under oxy-fuel conditions in a power plant boiler using CFD modelling. Fuel 2013;113:780–6. https://doi.org/10.1016/j.fuel.2013.03.075.

[21] Rabaçal M, Costa M, Vascellari M, Hasse C, Rieth M, Kempf A. A large eddy simulation study on the effect of devolatilization modelling and char combustion mode modelling on the structure of a large-scale, biomass and coal co-fired flame. J. Combust. 2018;2018:1–15. https://doi.org/10.1155/2018/7036425.

[22] Axt C, Pielsticker S, Kreitzberg T, Hatzfeld O, Gao Q, Li S, Kneer R. Simulative prediction of ultrafine particulate matter formation by means of different pyrolysis models. Fuel 2020;266. https://doi.org/10.1016/j.fuel.2019.116865. 116865.

[23] Niemelä NP, Tolvanen H, Saarinen T, Leppänen A, Joronen T. CFD based reactivity parameter determination for biomass particles of multiple size ranges in high heating rate devolatilization. Energy 2017;128:676–87. https://doi.org/10.1016/j.energy.2017.04.023.

[24] Björklund P, Joronen T, Bolhár-Nordenkampf M. Steam-exploded pellets for heat and power generation,. VGB PowerTech J 2016;4.

[25] W. H. Mason, Process and apparatus for disintegration of wood and the like (United States patent US 1578609, 1926).

[26] Björklund P, Material changes during steam explosion of bark, European Pellet Conference, Welch, Austria (1–2 March 2017).

[27] Singh J, Suhag M, Dhaka A. Augmented digestion of lignocellulose by steam explosion, acid and alkaline pretreatment methods: a review. Carbohydrate Polymers 2015;117:624–31. https://doi.org/10.1016/j.carbpol.2014.10.012.

[28] Valmet Oyj, Valmet to deliver the world's first BioTracTM steam explosion system for black pellet production in France [press release], link to press release (11 September 2018 [Accessed: 12 April 2019]).

[29] Abelha P, Vilela CM, Nanou P, Carbo M, Janssen A, Leiser S. Combustion improvements of upgraded biomass by washing and torrefaction. Fuel 2019;253: 1018–33. https://doi.org/10.1016/j.fuel.2019.05.050.

[30] Tolvanen H, Kokko L, Raiko R. Fast pyrolysis of coal, peat, and torrefied wood: Mass loss study with a drop-tube reactor, particle geometry analysis, and kinetics modeling. Fuel 2013;111:148–56. https://doi.org/10.1016/j.fuel.2013.04.030.

[31] Tolvanen H, Advanced solid fuel characterization for reactivity and physical property comparison, Ph.D. thesis, Tampere University of Technology, Publication, Vol. 1359, URL: http://URN.fi/URN:ISBN:978-952-15-3674-8 (1 2016).

[32] Tolvanen H, Keipi T, Raiko R. A study on raw, torrefied, and steam-exploded wood: Fine grinding, drop-tube reactor combustion tests in $N_2)/O_2$ and $CO_2)/O_2$ atmospheres, particle geometry analysis, and numerical kinetics modeling. Fuel 2016;176:153–64. https://doi.org/10.1016/j.fuel.2016.02.071.

[33] Rieth M, Large eddy and direct numerical simulation of single and multiphase flows relying on Lagrangian particle methods, Ph.D. thesis, University of Duisburg-Essen (2 2018).

[34] Johansen JM, Gadsbøll R, Thomsen J, Jensen PA, Glarborg P, Ek P, De Martini N, Mancini M, Weber R, Mitchell R. Devolatilization kinetics of woody biomass at short residence times and high heating rates and peak temperatures. Appl Energy 2016;162:245–56. https://doi.org/10.1016/j.apenergy.2015.09.091.

[35] Blondeau J, Jeanmart H. Biomass pyrolysis in pulverized-fuel boilers: Derivation of apparent kinetic parameters for inclusion in CFD codes. Proc Combust Inst 2011; 33:1787–94. https://doi.org/10.1016/j.proci.2010.06.150.

[36] ANSYS Fluent Theory Guide, release 15.0, Ansys Inc., Canonsburg, Pennsylvania, United States (November 2013).

[37] Magnussen BF, Hjertager BH. On mathematical models of turbulent combustion with special emphasis on soot formation and combustion. Symp (Int) Combust 1977;16:719–29. https://doi.org/10.1016/S0082-0784(77)80366-4.

[38] Li J, Bonvicini G, Tognotti L, Yang W, Blasiak W. High-temperature rapid devolatilization of biomasses with varying degrees of torrefaction. Fuel 2014;122: 261–9. https://doi.org/10.1016/j.fuel.2014.01.012.

[39] Gronli M, A theoretical and experimental study of the thermal conversion of biomass, Ph.D. thesis, Norwegian University of Science and Technology (11 1996).

[40] Haider A, Levenspiel O. Drag coefficient and terminal velocity of spherical and nonspherical particles. Powder Technol 1989;58:63–70. https://doi.org/10.1016/0032-5910(89)80008-7.

[41] Morsi SA, Alexander AJ. An investigation of particle trajectories in two-phase flow systems. J Fluid Mech 1972;55:193–208. https://doi.org/10.1017/S0022112072001806.

[42] Ganser GH. A rational approach to drag prediction of spherical and non-spherical particles. Powder Technol 1993;77:143–52. https://doi.org/10.1016/0032-5910(93)80051-B.

[43] Clift R, Grace JR, Weber ME. Bubbles, drops, and particles. New York: Academic Press; 1978.

[44] Ranz WE, Marshall Jr WR. Evaporation from drops: Part I. Chem Eng Prog 1952;48 (3):141–6.

[45] Johansen JM, Jensen PA, Glarborg P, Mancini M, Weber R, Mitchell RE. Extension of apparent devolatilization kinetics from thermally thin to thermally thick particles in zero dimensions for woody biomass. Energy 2016;95:279–90. https://doi.org/10.1016/j.energy.2015.11.025.

[46] Kleinhans U, Halama S, Spliethoff H. The role of gasification reactions during pulverized solid fuel combustion: A detailed char combustion model based on measurements of char structure and kinetics for coal and pre-treated biomass. Combust Flame 2017;184:117–35. https://doi.org/10.1016/j.combustflame.2017.05.033.

[47] Diaz-Mateus FA, Alvarez-Castro HC, Chaves-Guerrero A. CFD simulation of sugarcane bagasse combustion in an industrial grate boiler. DYNA 2018;85(204): 169–76. https://doi.org/10.15446/dyna.v85n204.65601.

[48] Li J, Brzdekiewicz A, Yang W, Blasiak W. Co-firing based on biomass torrefaction in a pulverized coal boiler with aim of 100% fuel switching. Appl Energy 2012;99: 344–54. https://doi.org/10.1016/j.apenergy.2012.05.046.

[49] Stubenberger G, Scharlerab R, Zahirović S, Obernberger I. Experimental investigation of nitrogen species release from different solid biomass fuels as a basis for release models. Fuel 2008;87:793–806. https://doi.org/10.1016/j.fuel.2007.05.034.